To appear in the *International Journal of Remote Sensing*
Vol. 00, No. 00, Month 20XX, 1–21

# Fourier-Mellin registration of two hyperspectral images

Álvaro Ordóñez[a], Francisco Argüello[b] and Dora B. Heras[a*]

[a] *Centro Singular de Investigación en Tecnoloxías da Información (CiTIUS), Universidade de Santiago de Compostela*;
[b] *Departamento de Electrónica e Computación, Universidade de Santiago de Compostela.*

(*Received 00 Month 20XX; accepted 00 Month 20XX*)

Hyperspectral images contain a great amount of information which can be used to more robustly register such images. In this paper, we present a phase correlation method to register two hyperspectral images that takes into account their multiband structure. The proposed method is based on principal component analysis, the multilayer fractional Fourier transform, a combination of log-polar maps, and peak processing. The combination of maps is aimed at highlighting some peaks in the log-polar map using information from different bands. The method is robust and has been successfully tested for any rotation angle with commonly used hyperspectral scenes in remote sensing for scales of up to 7.5× and with pairs of hyperspectral images taken on different dates by the Airborne Visible/Infrared Imaging Spectrometer (AVIRIS) sensor for scales of up to 6.0×.

**Keywords:** hyperspectral data; image registration; Fourier transform; feature extraction; remote sensing.

## 1. Introduction

The development of image sensor technology has made it possible to capture hyperspectral images composed of hundreds of bands covering a wide range in the electromagnetic spectrum (Landgrebe 2002). The high dimensionality of hyperspectral data offers new opportunities for recognizing and classifying materials. Applications range from agriculture (Haboudane et al. 2004), mineralogy (Cudahy et al. 2010), medicine, quality control, material inspection, and surveillance, among others. Hyperspectral sensors usually collect two dimensional spatial images comprising hundreds of spectral bands, so that specific techniques are required to exploit all the information available in the hyperspectral data (Fauvel et al. 2013).

Image registration is a fundamental task in many image processing applications. We consider the image registration problem associated with images where the translation, rotation, and scaling parameters between a reference image and a second image of the same scene must be estimated. Several different algorithms to solve automatic image registration have been proposed (Dawn, Saxena, and Sharma 2010; Deshmukh, and Bhosle 2011; Le Moigne, Netanyahu, and Eastman 2011; Goshtasby 2005, 2012). Fourier methods are very efficient because the fast Fourier transform (FFT) can be used to compute the cross-correlation (phase correlation) between

---

[*] Corresponding author. Email: dora.blanco@usc.es

the two images. Additionally, they are resilient to noise, occlusions, and other defects typical of medical or remote-sensing images. The method was proposed by Chen, Defrise, and Deconinck (1994) for translation, rotation and scale-invariant image registration using a log-polar grid. This method is also known as Fourier-Mellin invariant symmetric phase-only matched filtering (FMI-SPOMF) (Dasgupta and Chatterji 1996; Reddy and Chatterji 1996; Derrode and Ghorbel 2001). Keller, Averbuch, and Israeli (2005) introduce the pseudopolar Fourier transform (PPFT) to improve the approximation of the log-polar map for the estimation of large translations, rotations, and scalings. The pseudo-log-polar Fourier Transform (PLPFT), which can be calculated quickly by utilizing the Fourier separability property and the Fractional Fourier Transform (FRFT), was proposed by Liu, Guo, and Feng (2006). The PPFT was generalized by Chou, Izatt, and Farsiu (2009), while an octa-log-polar version of the PLPFT was proposed by Wu, Guo, and Wang (2009). A simpler approach was followed by Pan, Qin, and Chen (2009), who proposed an adaptable Multilayer Fractional Fourier Transform (MLFFT) for image registration with lower interpolation errors in both polar and log-polar grids.

Another approach in image registration is based on feature detection methods. These methods extract and match representative features from both images. The matched features between the two images allow determining the geometrical transformation that is needed to register the images. The Scale Invariant Feature Transform (SIFT) method was proposed by Lowe (2004) and presents a local descriptor that is robust to changes in illumination and camera viewpoint. It is invariant to image scaling or rotation. These characteristics make it an excellent approach for image registration, obtaining very effective algorithms (Rey Otero 2014; Ke, Yan, and Rahul Sukthankar 2004; Zhu et al. 2009). The Speeded-Up Robust Features (SURF) algorithm was proposed by Bay, Tuytelaars, and Van Gool (2006) and outperforms the SIFT method in terms of distinctiveness and computational time.

The hundreds of bands collected by a hyperspectral sensor can be acquired as a sequence of images at different wavelengths. Since it takes time to collect these images, image registration is required to match the band-to-band pixel locations and build coherent image cubes. For this purpose Kern, Pattichis, and Stearns (2004) used the multivariate mutual information as a similarity measure, while Moigne et al. (2002) developed methods based on wavelet decomposition, edge detection, mutual information and feature matching to perform dimension reduction and automatic registration and fusion of multisensor data. Fourier methods were implemented by Erives, and Fitzgerald (2005, 2006) to recover scaling, rotation, and translation parameters from an airborne hyperspectral imaging system. A similar system is proposed by Wang, Xu, and Zhang (2013). Vakalopoulou, and Karantzalos (2014) introduce an automated framework which allows using different feature descriptors such as SIFT, SURF and Affine-SIFT (ASIFT) to align the hyperspectral bands.

A slightly different task is the registration of two multi-channel images. Rhode et al. (2003) describe a general framework for the registration of two multi-channel images and propose a multivariate correlation as a similarity measure. However, most existing multi-channel image registration methods are specific to the registration of multi-valued medical data, such as phase contrast Magnetic Resonance Angiography (MRA) and diffusion tensor Magnetic Resonance Imaging (MRI). Ruiz-Alzola et al. (2002) proposed a unified framework for the nonrigid registration of 3D tensor medical data using local matching. The approach used by Avants (2008) is to average the cross-correlations calculated for each channel individually. Heinrich et al. (2014) present an approach based on canonical correlation analysis which is able to find new correlations using linear combinations of multiple channels.

In the field of remote sensing some methods have been proposed for the registration of two hyperspectral images. Mahdi and Farag (2002) use a genetic algorithm as a search technique to estimate the optimum parameters for the matching of two multispectral data sets. This approach can be considered a fusion of the different decisions resulting from the registration of the different bands. Chen, Leung, and Boss (2011) propose the use of the expectation maximization algorithm to solve the joint image registration and fusion problem. The registration parameters are estimated by maximizing a conditional expectation function. Bunting, Labrosse, and Lucas (2010) outline a method for the automatic registration of multi-sensor remote imagery using multiple scales and resolutions, introducing a self-organising network to control the movements of neighbouring tie points. However, none of these methods are based on Fourier transforms.

In this paper we propose a Fourier-based method for the registration of two hyperspectral images called HYperspectral Fourier-Mellin algorithm (HYFM). The method exploits the information contained in the different bands of the images and is based on principal component analysis, the multilayer fractional Fourier transform and a combination of log-polar maps. This last operation is aimed to highlighting some peaks in the log-polar map using information from different bands.

## 2. Registration of hyperspectral images

In this section we present an automatic method to register two hyperspectral images (reference and target) that exploits not only the spectral but also the spatial information available in the images. The proposed method is based on the computation of Fourier transforms and log-polar maps and on the processing of the peaks detected in these maps. The main problem that is successfully solved in this paper is the adaptation of the registration method to the case of hyperspectral images. When facing the processing of hyperspectral images, a key issue is that they are highly correlated in the spatial and spectral dimensions. This complicates the design of new algorithms and increases processing times.

In the case of the registration proposal presented here, the most direct approach is to perform the registration of each band of the two images separately and to compute a vote of the results obtained. This approach was discarded because of the excessive computational time and because the results are worse than using other solutions. A common approach in the literature in order to deal with the high dimensionality of the images is to perform a dimensionality reduction and feature extraction of the images by wavelets or Principal Component Analysis computation (PCA) (Richards 1999). The process, in this case registration, is then computed from a small number of components. The choice in this work is to retain typically four, eight, or the number of PCA components (PCs) required to accumulate "high enough" variance, for each one of the two images. The registration is then applied to pairs of PCA components.

In some experiments in this paper the dimensionality reduction is also carried out by computing a gradient of the hyperspectral image based on the Euclidean distances among pixel vectors by using the Robust Color Morphological Gradient (RCMG). This gradient (Evans and Liu 2006) reduces the dimensionality of each one of the original hyperspectral images so that finally a pair of one-band images whose edges are enhanced and thinned is obtained. In the experiments where the

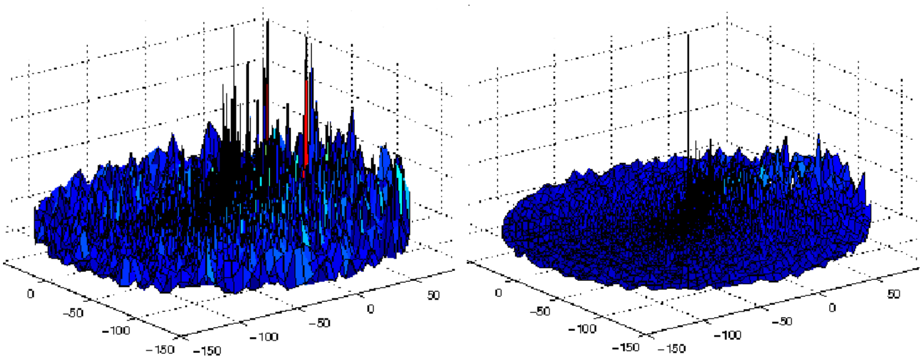

$(a)$ $(b)$

Figure 1. Log-polar maps after the phase correlation for two replicas of the Indian Pines image with a scale factor of 1 and a rotation angle of 45°: $(a)$ for the first PCA component, and $(b)$ for the combination of the first eight PCA components.

RCMG is calculated, a pair of components consisting of the RCMG band for each hyperspectral image is also included along with the PCA component pairs.

Additionally, the registration experiments performed have revealed that an efficient approach to combine the information is to combine the phase correlation maps computed for each pair of PCA components, since it allows each pair to contribute to the cross-correlation independently. The combination is performed by averaging the different contributions. The averaging of the log-polar maps is aimed at highlighting some peaks in the final map by using information from different bands. As an example, Figure 1 shows two log-polar maps after the correlation for two replicas of the Indian Pines image. On the left of the figure, the log-polar map is displayed for the first PC and a number of high peaks of similar height are observed, while the figure on the right shows the combination of phase correlations for the first eight PCA components where highlighted peaks are visible, especially one of them.

The registration method proposed in this paper, which it is called the HYFM method, is detailed in the pseudocode shown in Figure 2 and consists of the following steps. First, a PCA is performed on the two hyperspectral images retaining several components that are arranged in pairs. Next, the phase correlation method is applied to each pair of components. In this step, the MLFFT technique is used to approximate the log-polar grids. This technique uses Fractional Fourier Transforms (FRFTs) to reduce the interpolation errors and, therefore, to achieve better accuracy. Then, the different log-polar grids are combined to integrate the information from the different pairs of principal components. This step highlights some peaks of the log-polar grid. Finally, the highest peaks are examined to determine the scaling, rotation, and translation parameters. In the following subsections, we detail the different stages of the method.

### 2.1. *Phase correlation*

The Fourier based automatic registration relies on the Fourier shift theorem, which states that a circular shift in the spatial domain is equivalent to a phase ratio in the frequency domain.

Let $I_1(x, y)$ and $I_2(x, y)$ be two images, where $(x, y)$ are the spatial coordinates, being the second image a translated replica of the first one,

```
    Input: Two hyperspectral images (reference and target).
    Output: Scale factor $\rho_0$, rotation angle $\theta_0$, and shift $(x_0, y_0)$.
    Parameters: Number of components, FRFT $\alpha_l$ parameters, and number of log-polar peaks.
(1) Preprocessing (for the two images separately).
      (a) Apply a Blackman window to each hyperspectral band.
      (b) PCA computation.
      (c) Apply a high-pass filter to each component.
      (d) Extend each component to $N \times N$ pixels, with $N$ power of 2.
(2) Log-polar and phase correlation.
    • For each PCA component pair:
      (a) Compute FRFTs with parameters $\alpha_1, \alpha_2, \ldots, \alpha_L$ for each PCA component.
      (b) Compute the $L$-level MLFFT grid for each PCA component.
      (c) Approximate a $N/2 \times N/2$ log-polar grid for each PCA component.
      (d) Compute phase correlation in the log-polar grid.
(3) Combination of log-polar maps.
      (a) Average the log-polar maps obtained for each pair of PCA components.
(4) Peak processing.
      (a) Sort by magnitude the log-polar peaks.
          • For each peak (with coordinates $\rho'$ and $\theta'$):
             (i) Scale and rotate ($\theta'$ and $\theta' + \pi$) first PCA component of target image.
            (ii) Compute phase correlation in the cartesian grid.
           (iii) Select the highest peak (with coordinates $x'$ and $y'$).
      (b) Use the highest peak of all cartesian grids to determine $(\rho_0, \theta_0, x_0, y_0)$.
```

Figure 2. Pseudocode for the HYFM registration.

$$I_2(x, y) = I_1(x + x_0, y + y_0), \tag{1}$$

the shift theorem states that their Fourier transforms are related by

$$F_2(u, v) = \mathrm{e}^{i2\pi(ux_0 + vy_0)} F_1(u, v), \tag{2}$$

where $(u, v)$ are the coordinates in the transform space and $i$ is the imaginary unit.

Applying the phase correlation in the frequency domain,

$$\frac{F_1(u, v) F_2^*(u, v)}{|F_1(u, v) F_2^*(u, v)|} = \mathrm{e}^{-i2\pi(ux_0 + vy_0)}, \tag{3}$$

and, finally, computing the inverse Fourier transform, we obtain a matrix with approximate zeros everywhere except for a peak at coordinates $(x_0, y_0)$, that can be used to register the images.

To recover the rotation and scaling parameters, Chen, Defrise, and Deconinck (1994) proposed using the log-polar Fourier transform (Fourier-Mellin transform). Let $I_2$ be a translated, scaled, and rotated replica of $I_1$, with scale factor $\rho_0$ and rotation angle $\theta_0$, i.e.,

$$I_2(x, y) = I_1(\rho_0(x \cos\theta_0 + y \sin\theta_0 + x_0), \rho_0(-x \sin\theta_0 + y \cos\theta_0 + y_0)), \tag{4}$$

applying the Fourier shift theorem in polar coordinates $(\rho, \theta)$, we obtain,

$$F_2(\rho, \theta) = \mathrm{e}^{i(\omega_x x_0 + \omega_y y_0)} \rho_0^{-2} F_1(\rho_0^{-1}\rho, \theta + \theta_0), \tag{5}$$

where $\omega_x = \rho \cos\theta$ and $\omega_y = \rho \sin\theta$.

Moreover, taking the magnitude of the Fourier transform and the logarithm of the radius $\rho$, we have

$$|F_2(\ln \rho, \theta)| = \rho_0^{-2} |F_1(\ln \rho - \ln \rho_0, \theta + \theta_0)|, \tag{6}$$

wherein $\rho_0$ and $\theta_0$ can be obtained by applying again the Fourier shift theorem and the phase correlation. In this case, we obtain a matrix with approximate zeros everywhere except for a peak at coordinates $(\ln \rho_0, \theta_0)$, that can be used to register the images.

Stone, Tao, and McGuire (2003) investigated the factors that degrade the precision of image registration based on phase correlation. The major sources of error are interpolation error and rotationally dependent aliasing. Since rotationally dependent aliasing is exacerbated by the presence of high frequencies, the use of a Blackman window removes spurious high frequencies created by the image boundary and greatly reduces aliasing effects (Harris 1978). Since the remaining aliasing effects are strongest in the low frequencies of the Fourier transform, their effects can be reduced to a negligible amount by removing frequencies within a radius of $N/4$ of the Fourier domain origin. To this end, Reddy and Chatterji (1996) proposed using a simple high-pass emphasis filter transfer function based on the cosine function.

## 2.2. ***FRFT***

The Fractional Fourier Transform (FRFT) is a generalization of the discrete Fourier transform (DFT) whose exponent is modified by a parameter $\alpha$. The FRFT $\{G_k(\boldsymbol{x}, \alpha); 0 \leq k < m\}$ of a complex sequence of size $m$, $\boldsymbol{x} = \{x_j; 0 \leq j < m\}$, can be written as

$$G_k(\boldsymbol{x}, \alpha) = \sum_{j=0}^{m-1} x_j \mathrm{e}^{-2\pi i j k \alpha}. \tag{7}$$

$\alpha$ is not restricted to rational numbers and in fact may be any complex number. If $\alpha$ is a rational number, the FRFT can be reduced to a DFT and evaluated using conventional fast Fourier transforms (FFTs).

The FRFT can be efficiently computed by means of the fast algorithm described below (Bailey and Swarztrauber 1991). Suppose we wish to compute the FRFT for a complex sequence $\boldsymbol{x}$ of size $m$, where $m$ is a power of 2. Based on the "chirp $z$-transform" the FRFT expression can be derived as

$$G_k(\boldsymbol{x}, \alpha) = \mathrm{e}^{-\pi i k^2 \alpha} \sum_{j=0}^{2m-1} x_j \mathrm{e}^{-\pi i j^2 \alpha} \mathrm{e}^{\pi i (k-j)^2 \alpha} \tag{8}$$

$$= \mathrm{e}^{-\pi i k^2 \alpha} \sum_{j=0}^{2m-1} x_j y_j z_{k-j}, \tag{9}$$

where the $2m$-long complex sequences $\boldsymbol{y} = \{y_j; 0 \leq j < 2m\}$ and $\boldsymbol{z} = \{z_j; 0 \leq j < 2m\}$ are as follows

$$y_j = \mathrm{e}^{-\pi i j^2 \alpha}, \qquad 0 \leq j < m, \tag{10}$$

$$y_j = 0, \qquad m \leq j < 2m, \tag{11}$$

$$z_j = \mathrm{e}^{\pi i j^2 \alpha}, \qquad 0 \leq j < m, \tag{12}$$

$$z_j = \mathrm{e}^{\pi i (j-2m)^2 \alpha}, \qquad m \leq j < 2m, \tag{13}$$

and where

$$x_j = 0, \qquad m \leq j < 2m. \tag{14}$$

The $2m$-long sequences $\boldsymbol{y}$ and $\boldsymbol{z}$ satisfy the required property for a circular convolution, so DFTs may be used to evaluate (9):

$$G_k(\boldsymbol{x}, \alpha) = \mathrm{e}^{-\pi i k^2 \alpha} F_k^{-1}(\boldsymbol{w}), \qquad 0 \leq k < m, \tag{15}$$

where $\boldsymbol{w} = \{w_k; 0 \leq k < 2m\}$ is a $2m$-long sequence defined by $w_k = F_k(\boldsymbol{x} \odot \boldsymbol{y}) F_k(\boldsymbol{z})$, where $\odot$ denotes the element-wise multiplication, and $F$ and $F^{-1}$ denote the forward and inverse DFT. The remaining $m$ results of the final inverse DFT are discarded. In our case the data are centered by using an offset $s = m/2$, then we need to compute a different $m$-long sequence $G_{k+s}(\boldsymbol{x}, \alpha)$, $0 \leq k < m$. The expression for the FRFT (Equation 15) for the first $m$ values of $G_{k+s}(\boldsymbol{x}, \alpha)$ satisfies:

$$G_{k+s}(\boldsymbol{x}, \alpha) = \mathrm{e}^{-\pi i (k+s)^2 \alpha} F_{k+s}^{-1}(\boldsymbol{w}), \qquad 0 \leq k < m. \tag{16}$$

In this case $\boldsymbol{z}$ is as follows:

$$z_k = \mathrm{e}^{\pi i (k+s)^2 \alpha}, \qquad 0 \leq k < m, \tag{17}$$

$$z_k = \mathrm{e}^{\pi i (k+s-2m)^2 \alpha}, \qquad m \leq k < 2m. \tag{18}$$

This procedure is referred to as the FRFT transform algorithm.

Figure 3 shows the computation of the FRFT applied to a 2-dimensional image $\mathbf{X}$ instead of a sequence $\boldsymbol{x}$ ($G(\mathbf{X}, \alpha)$). Equation 16 must be calculated and, as the FRFT is a separable operation, the 2D fractional Fourier transform (2D-FRFT) can be expressed as a product of two functions operating separately by rows and by columns. To calculate the 2D-FRFT, first, we apply a 1D fractional Fourier transform (Equation 16) to each row and then we apply a 1D fractional Fourier transform to each column. This is simplified by performing the element-wise multiplications by rows and columns in the same step, reusing data and saving computation time, as illustrated in the first, third and last steps in Figure 3, where $*$ denotes the complex conjugate and T the transpose of a matrix.

In the first step (beginning on the left of Figure 3) the FFT of the element-wise multiplication of the image $\mathbf{X}$ and the sequence $\boldsymbol{y}$ is calculated, that is, $F_k(\boldsymbol{x} \odot \boldsymbol{y})$. Also the FFT of $\boldsymbol{z}$ is computed in the second step. Then, in the third step, $w_k =$

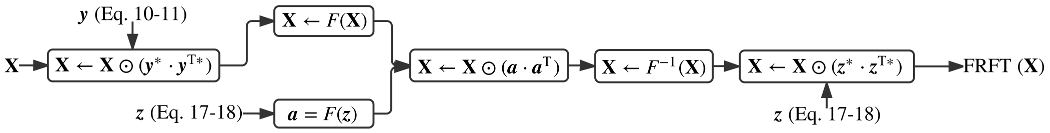

Figure 3. Flowchart of the FRFT computation of an image $\mathbf{X}$.

$F_k(\boldsymbol{x} \odot \boldsymbol{y})F_k(\boldsymbol{z})$ for $0 \leq k < m$ is calculated also operating by rows and by columns. Next, in the fourth step, the inverse Fourier transform of the previous multiplication ($F^{-1}_{k+s}(\boldsymbol{w})$) is computed. In the last step, the multiplications of the result of the previous step by $\mathrm{e}^{-\pi i(k+s)^2\alpha}$ are calculated. This corresponds to the right side of Equation 16, $F^{-1}_{k+s}(\boldsymbol{w})$. As a result, the FRFT of the image $\mathbf{X}$ is obtained. From a computational point of view, it can be observed that the terms $\mathrm{e}^{-\pi i(k+s)^2\alpha}$ are equal to the first range of $\boldsymbol{z}$ that was previously calculated (see Equation 18). The sequences $\boldsymbol{z}$ and $\boldsymbol{y}$ and the transform $F_k(\boldsymbol{z})$ are precomputed in order to reuse them consequently saving computation time. The computation of the 2D-FRFT requires the computation of 3 2D-FFT of double size, so the complexity of the 2D-FRFT is the same as for a 2D-FFT, i.e., $\mathrm{O}(m^2 \log_2 m)$.

### 2.3. *MLFFT*

As we discussed in Section 2.1, log-polar maps and phase correlation computations are the base for obtaining the scale factor and the rotation angle in the Fourier-Mellin registration method. Rotation aliasing is an important source of error that is difficult to overcome, thus scaling overlapping will be inevitable and critical for registering images with large-scale factors. The main challenge is to evaluate the log-polar Fourier transform efficiently and accurately, and different ideas have been proposed in recent years to solve this problem. These include the pseudo-polar (Keller, Averbuch, and Israeli 2005), pseudo-log-polar (Liu, Guo, and Feng 2006), generalized pseudo-polar (Chou, Izatt, and Farsiu 2009), and the octa-log-polar (Wu, Guo, and Wang 2009) maps, among others. We use the MLFFT (Pan, Qin, and Chen 2009), since it has lower interpolation errors in both polar and log-polar grids, and can be computed efficiently. Recovering scale factors of up to 5 with arbitrary rotation angles or scale factors of up to 10 without rotation in gray-level images have been reported by different authors.

The MLFFT uses a multilevel grid to approximate the log-polar grid, as illustrated in Figure 4. Since the point spacing in the log-polar map follows a logarithmic law relative to the radius, MLFFT uses a denser grid in the lower levels. Each level of the MLFFT can be computed by means of a FRFT with a particular parameter $\alpha_l$ as described in Section 2.2, which requires three FFTs of size $2N$ for computing one FRFT of size $N$. Then, the $L$-level MLFFT grid can be written as

$$\boldsymbol{P} = \bigcup_{l=1}^{L} \boldsymbol{P}_l \tag{19}$$

where $\boldsymbol{P}_l = \{P_{l_p}; 0 \leq p < N\}$, $P_{l_p} = G_p(\boldsymbol{x}, \alpha_l)$, $\boldsymbol{x}$ is a row or column of matrix $\mathbf{X}$, and $0 < \alpha_1 < \alpha_2 < \cdots < \alpha_L = 1$. $P_{l_p}$ is first calculated for all the $N$ rows of $\mathbf{X}$ and then for all the $N$ columns. Usually, a number of levels $L$ between two and four is used.

Figure 5 describes a computation of a four-level MLFFT over an image, in this

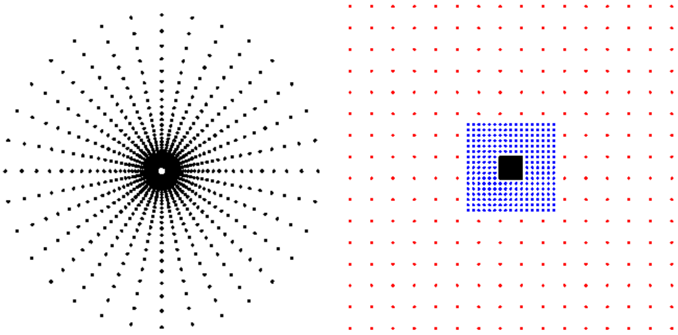

(*a*) (*b*)

Figure 4. Grids: (*a*) log-polar, and (*b*) MLFFT.

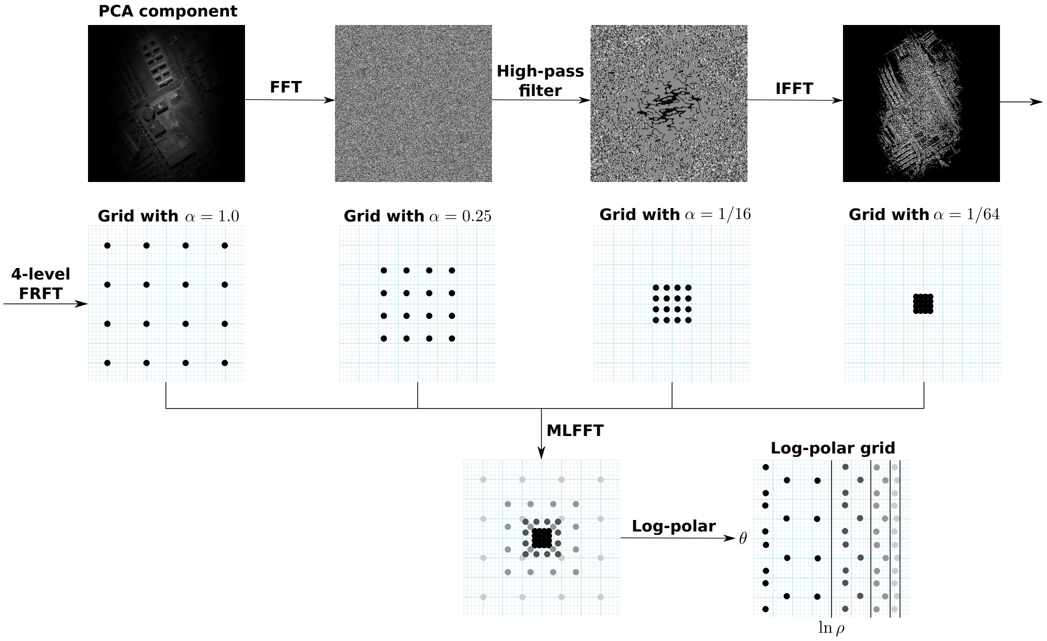

Figure 5. Computation of a four-level MLFFT over a PCA component.

case a PCA component of a hyperspectral image. First, a high-pass filter is applied to remove aliasing effects, as we discussed in Section 2.1. It involves applying a FFT, the filter and finally the inverse Fourier transform as can be seen in the top part of the figure. Secondly, four FRFTs with $\alpha = \{1, 1/4, 1/16, 1/64\}$ are computed (the bottom part of the figure). Using Equation (19) the MLFFT grid is calculated. The points in each level are represented in different gray levels. Finally, the log-polar grid is generated by interpolating on the MLFFT grid.

### 2.4. *Peak processing*

Once the phase correlation and the combination of maps of the different pairs of PCA components have been performed, a log-polar map is obtained with approximate zeros everywhere except for several peaks. In the ideal case, there will be a single peak at the coordinates corresponding to the scale factor and the rotation angle. However, in real applications, we will have more than one peak in the result. This is due to the interpolation errors and rotationally dependent aliasing, as well as due to the fact that the images do not match exactly. If undesirable large false peak values occur, the FFT-based algorithm may be unsuccessful in registering the images. Therefore, it is advisable to have a procedure capable of identifying the true peak.

The Fourier-Mellin registration process has two stages: phase correlation in the log-polar map to detect the scale factor and the rotation angle, and phase correlation in the cartesian grid (after correcting the scaling and rotation of the target image) to determine the translation. In order to find the best peak in the combined correlation map in the proposed method for hyperspectral images, as shown in the pseudocode at Figure 2, all the highest peaks in the log-polar map are processed. The second phase of correlation in the cartesian grid is then used to select the best peak, producing very good results. First, the peaks in the log-polar map are sorted by magnitude and the higher value ones are processed. The coordinates of each peak determine a tentative scale factor $\rho'$ and rotation angle $\theta'$ (due to the ambiguity of the log-polar map, it is necessary to examine also the angle $\theta' + \pi$). Next, the first component of the target image is scaled and rotated, and phase correlation is performed on the cartesian grid to determinate the translation parameters. A peak in the cartesian grid will be obtained for each pair of $\rho'$ and $\theta'$ values. The value of the highest peak in the cartesian grid will determine the correct peak in the log-polar grid. Finally, the coordinates of this selected peak in the log-polar map determine the scale factor $\rho_0$ and the rotation angle $\theta_0$, while the peak coordinates in the cartesian grid determine the translation parameters $(x_0, y_0)$.

## 3. Evaluation

Seven hyperspectral scenes were used to evaluate the method proposed in this work. The first four images are single datasets commonly used for testing in the field of remote sensing. The remaining scenes are pairs of datasets taken on different dates.

### 3.1. *Test images*

These scenes were taken by the ROSIS (Reflective Optics System Imaging Spectrometer) and AVIRIS (Airborne Visible/Infrared Imaging Spectrometer) sensors and are commonly used for testing in remote sensing (EHU 2015). Ground reference data are available for these images, which are displayed in Figure 6. The ROSIS-03 sensor captures 115 bands in the spectral range from 0.43 to 0.86 µm, corresponding mainly to the visible spectrum. The AVIRIS sensor captures 224 bands in the spectral range from 0.4 of 2.5 µm, corresponding to the visible and infrared spectrum. For these scenes, the registration is performed with a rotated and scaled version of the same image. The reason for registration with the same image is that all the details can be investigated in a controlled environment.

The first dataset is the Pavia University image. It is a ROSIS image of 103 bands (the twelve noisiest bands were removed) of the urban area surrounding the University of Pavia, Italy. Its location is latitude N 45°12'13.176" and longitude E 9°8'11.108". The image size is 610 × 340 pixels with a spatial resolution of 1.3 m per pixel. The pixels in the ground reference data are assigned to one out of nine classes: asphalt, meadows, gravel, trees, metal sheets, bare soil, bitumen, bricks, and shadows.

The second ROSIS dataset is the Pavia Centre image, and it is located at latitude N 45°11'07.4" and longitude E 9°8'34.8". It was originally $1096 \times 1096$ pixels in size, but a 381-pixel-wide black vertical band in the middle of the image was removed,

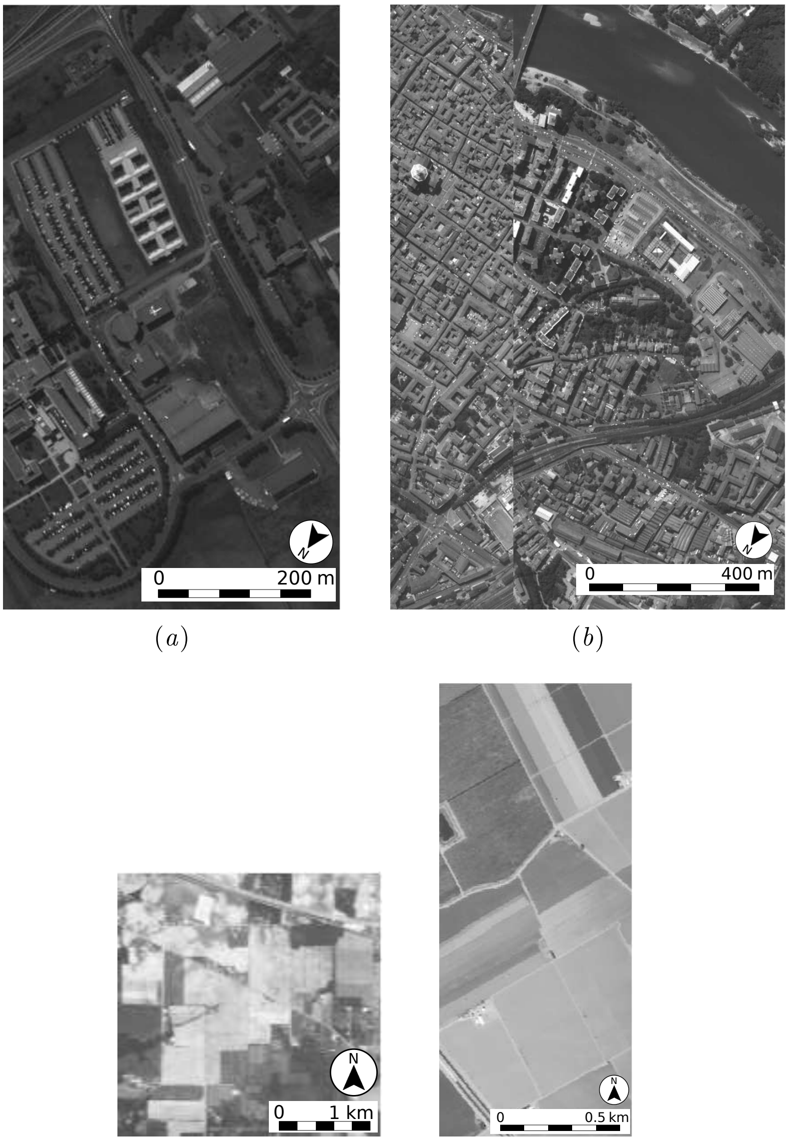

(*a*) (*b*)

(*c*) (*d*)

Figure 6. Hyperspectral images commonly used for testing in remote sensing: (*a*) Pavia University, (*b*) Pavia Centre, (*c*) Indian Pines, and (*d*) Salinas.

resulting in a two-part image of 1096 × 715 pixels. Thirteen channels have been removed due to noise, leading to an image of 102 bands with a spatial resolution of 1.3 m per pixel. Nine classes of interest are considered: water, trees, meadows, bricks, soil, asphalt, bitumen, tiles, and shadows.

The third dataset is a 220-band AVIRIS image (four bands were removed) taken over the Indian Pines Test Site 3 (2 × 2 mile portion of NW Tippecanoe County, Indiana). Details on the location of this image can be found in Gualtieri et al. (1999). This image has a size of 145 × 145 pixels and a spatial resolution of 20 m per pixel. The scene is a rural area which contains two-thirds agriculture (alfalfa, corn, grass, oats, soybean, wheat) and one-third forest or other natural perennial vegetation. There are two major dual lane highways, smaller roads, a rail line, some low density housing and other built structures.

The fourth dataset was collected by the AVIRIS sensor over Salinas Valley in

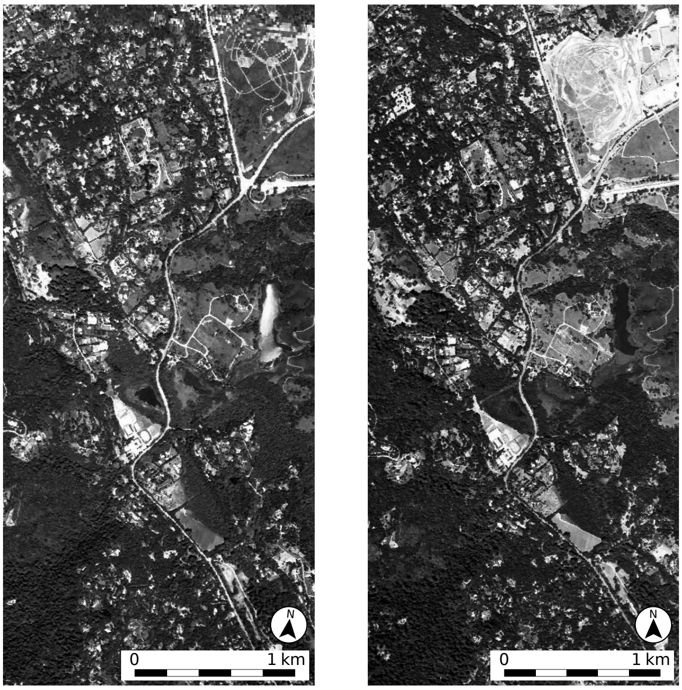

(*a*) (*b*)

Figure 7. Jasper Ridge Biological Preserve 1 scene taken by the AVIRIS sensor. (*a*) 588 × 1286 pixel fragment of the first image taken on 12 May 2006, and (*b*) fragment of the second image taken on 13 August 2007 with the same number of pixels.

Central California. More details about the location of this image can be found in Gualtieri et al. (1999). It is an image of a rural scene with a size of $512 \times 217$ pixels and 204 spectral bands (after elimination of water absorption and noisy bands). It was taken at low altitude with a pixel size of 3.7 m. The scene includes crops in different stages of growth (broccoli, lettuce, corn, celery), stubble, bare soils and vineyard fields.

### 3.2. *Pairs of images taken at different dates*

The remaining scenes are pairs of images taken by the AVIRIS sensor at different dates. Each pair of images, in addition to different scaling and orientation factors, presents differences in the lighting conditions, changes in vegetation, and alterations in buildings and infrastructures. To increase the range of the study, we have performed additional operations of scaling and rotation over the second image of each pair. These images were loaded from the AVIRIS database (Aviris 2015) and no additional processing or band removal was performed.

The Jasper Ridge Biological Preserve 1 scene covers a region of the nature preserve and biological field station of Jasper Rigde, CA. Its location is latitude N 37°24'8.5" and longitude W 122°14'42.2". It includes a wooded part as well as one more open with vegetation, ponds, bare soil, roads and some buildings. The first image of the pair was taken in a time of strong growth of vegetation, while the second, taken a year later, has a drier appearance. The pixel size is 3.3 m for the first image and 3.4 m for the second one. A region of 588 × 1286 pixels from both images was selected. They are shown in Figure 7.

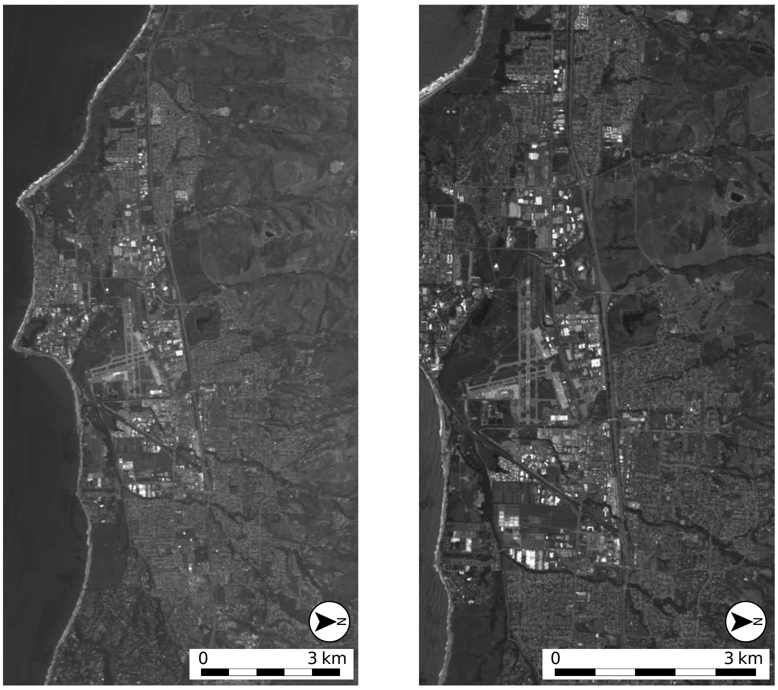

($a$) ($b$)

Figure 8. Santa Barbara Front Range A2 scene taken by the AVIRIS sensor. ($a$) 470×900 pixel fragment of the first image taken on 30 March 2009, and ($b$) fragment of the second image taken on 30 April 2010 with the same number of pixels.

The sixth scene, Santa Barbara Front Range A2, shows a section of the town of Santa Barbara, CA. It is located at latitude N 34°26'24.3" and longitude W 119°50'40.0". It includes an urban area with numerous buildings and structures and some vegetation, in addition to the coastline. Both images, which were taken with an interval of one year, differ in the spatial resolution, which is 16.4 m for the first image and 11.3 m for the second one. The selected region, shown in Figure 8, contains $470 \times 900$ pixels.

The last scene corresponds to Santa Barbara Box Line 8 (SB31), a crop area next to Santa Barbara, CA, delimited by a mountainous area. It is located at latitude N 35°18'14.3" and longitude W 118°50'22.6". The first image was taken in clear weather, while the second, taken a year later, presents a few clouds. The spatial resolution of both images is similar, 15.2 m per pixel. A region of $769 \times 1024$ pixels was selected from both images, as shown in Figure 9.

### 3.3. *Procedure and results*

The HYFM algorithm was programmed in C and comprises four main functions: computation of PCA, FRFT and MLFFT grid, phase correlation, and peak processing. Bicubic interpolation was used to approximate the log-polar grid and to rotate and scale the images. The algorithm has three selectable parameters: the number the components to retain in the PCA (eight components in our case), the $\alpha_l$ parameters in the FRFT and MLLFT ($\{1, 1/4, 1/16, 1/64\}$), and the number of log-polar peaks to be examined (50).

The procedure used to test the method is as follows. The first image of each pair is used as a reference while the target image is rotated and scaled. We have carried

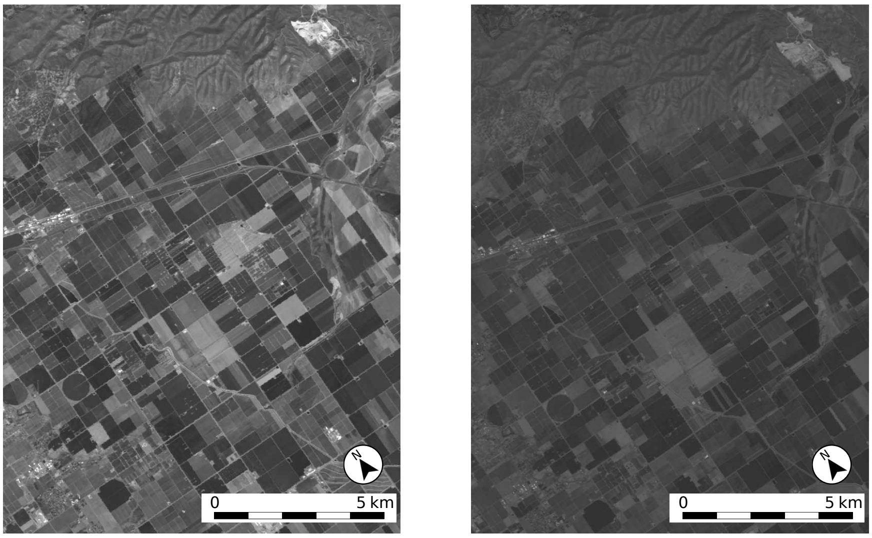

(*a*) (*b*)

Figure 9. Santa Barbara Box Line 8 scene taken by the AVIRIS sensor. (*a*) 769 × 1024 pixel fragment of the first image taken on 11 April 2013, and (*b*) fragment of the second image taken on 16 April 2014 with the same number of pixels.

(*a*) (*b*) (*c*)

Figure 10. Example of registration process: (*a*) original or reference image, (*b*) target image (central region of the original image scaled by 5.5× and rotated 45°), and (*c*) result of the registration process showing the correctly registered superposition of the reference and target image.

out exhaustive search with scale factors ranging from 1/6× to 8× (20 scale factors) and rotation angles from 0° to 360° in increments of 5° (72 angles). Two types of experiments are considered: in the first type the target image is scaled down (scale factors of $1/i\times,\ i = 6, 5, \ldots, 2$) while in the second one it is scaled up (scale factors of 1× to 8× in steps of 0.5×) while the scene is trimmed on the central region to keep the number of pixels constant, as can be seen in Figure 10. This second case is more realistic because it corresponds to the images taken by a sensor at different distances and orientations, as shown in the image pairs of Figures 7, 8, and 9.

First of all, we have compared two different configurations of the proposed HYFM

Table 1. Successfully registered cases for each scene using two variants of the proposed HYFM method.

| Scene | HYFM (4 PCAs + RCMG) | Proposed HYFM (8 PCAs) |
|---|---|---|
| Pavia Univ. | 1/4× to 5.5× | 1/4× to 5.5× |
| Pavia Centre | 1/6× to 7.5× | 1/5× to 7.5× |
| Indian Pines | 1/2× to 3.0× | 1/2× to 4.0× |
| Salinas | 1/2× to 4.5× | 1/2× to 4.5× |
| Jasper Ridge | – | 1/5× to 3.0× |
| Santa Barbara Front | 1/4× to 3.5× | 1/4× to 3.5× |
| Santa Barbara Box | 1/4× to 5.0× | 1/4× to 6.0× |

method as shown in Table 1. The first configuration (denoted as HYMF (4 PCA components + RCMG) in the table) considers five components of each image over which the registration is performed. These include the four most relevant PCs generated by PCA and a gradient of the image calculated by using RCMG. The second version of the proposed algorithm considers more components, in particular, eight PCA components and does not include the RCMG of the images. It is important to note that for the pairs of images taken by the AVIRIS sensor at different dates (see Figures 7, 8, and 9) to increase the range of the study we have performed additional operations of scaling and rotation over the second image of each pair.

Table 1 summarizes the correctly registered cases for each scene considering these two versions. In both cases the same parameters were used (bicubic interpolation, same number of peaks, the same MLLFT parameters, etc.). This was also the case in the following comparisons. Although for the largest part of the images both configurations show the same results, there are two images for which the results are different. For Indian Pines (IP), the second configuration successfully registers two more cases than the first configuration, specifically for 3.5× and 4.0×. For the Jasper Ridge image (JR) the registration is unsuccessful for all the cases when the first configuration is used. The reason is that the information retained by the RCMG is not enough for this complex image. Thus, the second configuration of the proposed method is selected for the remainder of the paper.

Table 2 shows the registration details for the proposed method. Note that the scaling of 1× corresponds to the registration of pairs of images without scaling. For this scaling for all images, including those taken at different dates for the same scene, the registrations are successful for all angles.

### 3.4. *Comparison with other methods*

The Fourier-Mellin algorithm has been used as the basis for several registration methods. For gray-level images, the best result reported using the PPFT (Keller, Averbuch, and Israeli 2005), PLPFT (Liu, Guo, and Feng 2006), generalized PPFT (Chou, Izatt, and Farsiu 2009) and octa-log-polar PLPFT (Wu, Guo, and Wang 2009) estimate scale factors of up to 4× and arbitrary rotation angles. The MLFFT (Pan, Qin, and Chen 2009) is able to recover scale factors of up to 5× with arbitrary rotation angles, as reported by the authors. The method we propose in this work has been successfully tested for any rotation angle with commonly used hyperspectral scenes in remote sensing for scalings of up to 7.5× and with pairs of hyperspectral images taken on different dates by the AVIRIS sensor for scalings of up to 6.0×.

Regarding the registration of hyperspectral images, the Fourier-Mellin algorithm has been used to match the band-to-band pixel locations and build coherent image cubes in airborne hyperspectral imaging systems (Erives, and Fitzgerald 2005,

Table 2. Registration details for the proposed HYFM method over the Pavia Centre (PC), Pavia Univ. (PU), Santa Barbara Box Line (SBB), Salinas (S), Indian Pines (IP), Jasper Ridge (JR), and Santa Barbara Front Range (SBF) scenes. For each scale factor the rate of angles with successful registration (in percentage) is indicated (for a total of 72 angles in steps of 5°).

| | Rate of angles (%) | | | | | | |
|---|---|---|---|---|---|---|---|
| Scale factor | PC | PU | SBB | S | IP | SBF | JR |
| 1.0 – 3.0× | 100 | 100 | 100 | 100 | 100 | 100 | 100 |
| 3.5× | 100 | 100 | 100 | 100 | 100 | 100 | 88 |
| 4.0× | 100 | 100 | 100 | 100 | 100 | 83 | 67 |
| 4.5× | 100 | 100 | 100 | 100 | 93 | 39 | 14 |
| 5.0× | 100 | 100 | 100 | 90 | 46 | 0 | 3 |
| 5.5× | 100 | 100 | 100 | 78 | 21 | 0 | 0 |
| 6.0× | 100 | 75 | 100 | 65 | 0 | 0 | 0 |
| 6.5× | 100 | 44 | 75 | 40 | 0 | 0 | 0 |
| 7.0× | 100 | 28 | 49 | 19 | 0 | 0 | 0 |
| 7.5× | 100 | 19 | 8 | 1 | 0 | 0 | 0 |
| 8.0× | 61 | 19 | 7 | 0 | 0 | 0 | 0 |

2006; Wang, Xu, and Zhang 2013). In these cases, the registration is carried out band-to-band and the scale factors of required are close to unity. For the registration of multimodal remotely sensed datasets several methods have been proposed (Mahdi and Farag 2002; Chen, Leung, and Boss 2011; Bunting, Labrosse, and Lucas 2010), but they are intended for the recovering of linear and non-linear translations and small scalings and rotations, both global and local. We are not aware of published Fourier-Mellin based methods aimed at the recovery of large scalings in pairs of hyperspectral images.

As mentioned in Section 1, feature-based methods provide good registration results due to their invariance to changes in illumination, rotation and scaling. For this reason, such methods have been compared to the proposed method. Table 3 summarizes the cases that were correctly registered for each scene by the proposed scheme with the best configuration of Table 1 as compared to to the results in the literature. The first five columns display the results for previously published methods using the first PCA component of the hyperspectral image. The first and second columns show the results for the original Fourier-Mellin (FMI-SPOMF) (Chen, Defrise, and Deconinck 1994) and MLLFT (Pan, Qin, and Chen 2009) methods, while the third, fourth and fifth columns make reference to feature extraction algorithms, specifically SURF (Bay, Tuytelaars, and Van Gool 2006) and two SIFT implementations: the original (SIFT-1) (Lowe 2004) and a more recent version (SIFT-2) (Rey Otero 2014). The sixth column shows the results for the proposed HYFM method considering eight PCA components. The same parameters were used in all methods based on the FFT (bicubic interpolation, same number of peaks, the same parameters for the MLLFT, etc.). The same holds for the three feature extraction algorithms used (the same algorithm for matching the feature points, the same method to estimate the global affine transformation model, etc.). Due to the arbitrariness of the Random Sample Consensus (RANSAC) algorithm, in order to estimate the model parameters in these three methods, 50 executions were carried out for each case. Even though the FMI-SPOMF and MLLFT methods present very similar results in Table 3, the second one is more robust since it needs fewer peaks to produce the same result and the number of rotation angles that failed is smaller. SURF is not stable to rotation changes, as shown in the table by the fact that it achieves correct registrations for only a small number of scalings.

The proposed HYFM method provides the best results on average, correctly

Table 3. Successfully registered cases for each scene. The number in parentheses indicates the number of scalings that were correctly registered for all angles. Proposed HYFM refers to HYFM (8 PCAs) while FMI-SPOMF, MLFFT, SURF, SIFT-1 and SIFT-2 are applied to the first PCA component of each image.

| Scene | FMI-SPOMF | MLLFT | SURF |
|---:|---:|---:|---:|
| Pavia Univ. | 1/4× to 4.5× (11) | 1/4× to 4.5× (11) | 1/4× to 3.0× (8) |
| Pavia Centre | 1/5× to 6.0× (15) | 1/5× to 6.0× (15) | 1/6× to 5.5× (15) |
| Indian Pine | 1/2× to 3.0× (6) | 1/2× to 3.0× (6) | 1.0× (1) |
| Salinas | 1/2× to 4.0× (6) | 1/2× to 4.0× (6) | 1/2× to 1.5× (3) |
| Jasper Ridge | 1/3× to 2.5× (6) | 1/3× to 2.5× (6) | (0) |
| Santa Barbara Front | 1/4× to 2.5× (7) | 1/4× to 2.5× (7) | 1.0× (1) |
| Santa Barbara Box | 1/2× to 2.0× (4) | 1/3× to 2.0× (5) | 1.0× (1) |
| Average number of scalings | (7.86) | (8.00) | (4.14) |

| Scene | SIFT-1 | SIFT-2 | Proposed HYFM |
|---:|---:|---:|---:|
| Pavia Univ. | 1/6× to 5.5× (15) | 1/2× to 2.0× (4) | 1/4× to 5.5× (13) |
| Pavia Centre | 1/8× to 6.5× (19) | 1/5× to 2.5× (8) | 1/5× to 7.5× (18) |
| Indian Pine | 1/3× to 3.0× (7) | 1/2× to 1.0× (2) | 1/2× to 4.0× (8) |
| Salinas | 1/4× to 5.5× (13) | (0) | 1/2× to 4.5× (9) |
| Jasper Ridge | (0) | 1/2× to 1.5× (3) | 1/5× to 3.0× (9) |
| Santa Barbara Front | 1.0× to 1.5× (2) | 1/3× to 8.0× (17) | 1/4× to 3.5× (9) |
| Santa Barbara Box | 1/3× to 1.5× (4) | 1/2× to 1.0× (2) | 1/4× to 6.0× (14) |
| Average number of scalings | (8.57) | (5.14) | (11.43) |

registering 11.43 cases versus 8.57 for SIFT-1. As discussed before, MLFFT is slightly more robust than the original FMI-SPOMF method, registering 8.00 cases versus 7.86. The SIFT-2 and the SURF methods provide worse results, as only 5.14 and 4.14 cases, respectively, have been correctly registered.

In general, SIFT-1 achieves slightly better results when the target image is a scaled and rotated version of the original image, but it fails to register pairs of hyperspectral images taken on different dates. For the Jasper Ridge image, SIFT-1 registers all cases incorrectly, while for the Santa Barbara images the number of correctly registered cases is very low. The SIFT-2 implementation provides worse results than SIFT-1, except for the Santa Barbara Front in which this method achieves the best results. The limited capacity of these methods to register different images could be due to the fact that the identification of keypoints is sensitive to small changes in the image.

The proposed HYFM method provides good results for all the scenes. The best results are obtained for the pairs of hyperspectral images taken on different dates by the AVIRIS sensor. For example, for the Jasper Ridge scene, scalings of 3.0× have been recovered, while other methods have failed due to small structures that are difficult to register.

In terms of registration error, the average error rate in angles and scalings for each scene are presented in Table 4 for the best two methods, i.e., HYFM and SIFT-1. The error rates have been calculated over the cases that were successfully registered by both methods. The proposed HYFM method provides lower error rates in angles and scalings for all the scenes. These results confirm that the HYFM method aligns hyperspectral images with higher accuracy.

## 4. Conclusions

In this paper we have proposed a Fourier-Mellin algorithm to register two hyperspectral images and evaluated its results on several datasets used in remote sensing for land-cover applications. The method is based on principal component analysis, the multilayer fractional Fourier transform, a combination of log-polar maps, and peak processing. The Fourier transform is computed through the FRFT over a multilayer grid, which reduces the interpolation errors in the log-polar map. In

Table 4. Average error rate in percentage for angles and scalings for the successfully registered cases for each scene using the HYFM and SIFT-1 methods.

| | Angle error (%) | | Scalings error (%) | |
|---|---|---|---|---|
| | HYFM | SIFT-1 | HYFM | SIFT-1 |
| Pavia Univ. | 0.26 | 1.33 | 0.38 | 0.95 |
| Pavia Centre | 0.17 | 0.96 | 0.27 | 0.56 |
| Indian Pines | 1.00 | 1.14 | 0.66 | 1.38 |
| Salinas | 0.57 | 1.67 | 0.52 | 0.93 |
| Jasper Ridge † | 0.21 | 77.56 | 0.56 | 77.50 |
| Santa Barbara Front | 0.39 | 2.20 | 0.15 | 0.82 |
| Santa Barbara Line | 0.23 | 2.13 | 0.19 | 0.85 |

† For Jasper Ridge the cases successfully registered by HYFM have been used.

addition, it can be efficiently computed.

The proposed registration method takes into account the multiband structure of the hyperspectral images. This is achieved through two strategies: the images are first processed using PCA, enabling dimensionality reduction and feature extraction. Second, the combination of log-polar maps is applied after the phase correlation, which allows each pair of components to contribute independently to the crosscorrelation. This stage is aimed at highlighting some peaks in the log-polar map using information from different bands. A final peak processing stage is applied to discriminate the false peaks due to interpolation errors and rotationally dependent aliasing, as well as the images that do not match exactly.

We have performed several experiments on four hyperspectral images that are commonly used for testing in remote sensing (Pavia Univ., Pavia Centre, Indian Pines, and Salinas), as well as three pairs of remote sensing hyperspectral images taken by the AVIRIS sensor on different dates (Jasper Ridge Biological Preserve 1, Santa Barbara Front Range A2, and Santa Barbara Box Line 8 (SB31)). These images correspond to rural and urban scenes and contain various types of crops, forests and other natural vegetation, buildings, asphalt, etc. The last three pairs of images, in addition to different scaling and orientation factors, present differences in the lighting conditions, changes in vegetation, and alterations in buildings and infrastructures. The proposed method has been compared to the FMI-SPOMF, MLFFT, SIFT and SURF methods available in the literature. The results show successful registration for more images and scalings for the proposed method while presenting lower error rates. For example, a scale factor of 6.0× has been recovered in Santa Barbara Box Line by the HYFM method with an error rate in angles and scalings of 0.23% and 0.19%, respectively. For the SIFT method a scale factor of 1.5× with error rates of 2.13% and 0.85% was obtained.

## Supplemental data

The underlying research materials for this article can be accessed at `https://wiki.citius.usc.es/hiperespectral:HYFM-REG`.

## Acknowledgements

This work was supported in part by the Ministry of Science and Innovation, Government of Spain, cofunded by the FEDER funds of European Union [grant numbers TIN2013-41129-P and TIN2016-76373-P] and by Xunta de Galicia, Programme for

Consolidation of Competitive Research Groups [grant number 2014/008].

## References

Avants, B. B., C. L. Epstein, M. Grossman, and J. C. Gee. 2008. “Symmetric diffeomorphic image registration with cross-correlation: evaluating automated labeling of elderly and neurodegenerative brain.” *Medical image analysis* 12 (1): 26-41.

AVIRIS database. 2015. [Online]. Available: [`http://aviris.jpl.nasa.gov/data/index.html`] (2015, June).

Bailey, David H., and Paul N. Swarztrauber. 1991. “The Fractional Fourier Transform and Applications.” *SIAM Review* 33 (3): 389-404.

Bay, Herbert and Tuytelaars, Tinne and Van Gool, Luc. 2006. “Surf: Speeded up robust features.” *European conference on computer vision* 404-417.

Bunting, P., F. Labrosse, and R. Lucas. 2010. “A multi-resolution area-based technique for automatic multi-modal image registration.” *Image and Vision Computing* 28 (8): 1203-1219.

Chen, Q. S., M. Defrise, and F. Deconinck. 1994. “Symmetric phase-only matched filtering of Fourier-Mellin transforms for image registration and recognition.” *Pattern Analysis and Machine Intelligence, IEEE Transactions on* (16) 12: 1156-1168.

Chen, S., Q. Guo, H. Leung, and Boss. 2011. “A maximum likelihood approach to joint image registration and fusion.” *Image Processing, IEEE Transactions on* (20) 5: 1363-1372.

Chou, N., J. Izatt, and S. Farsiu. 2009. “Generalized pseudo-polar Fourier grids and applications in registering ophthalmic optical coherence tomography images.” In *Signals, Systems and Computers, Conference Record of the Forty-Third Asilomar Conference on, ACSSC 2009* 807-811.

Cudahy, T., M. Jones, M. Thomas, P. Cocks, F. Agustin, M. Caccetta, R. Hewson, M. Verrall, and A. Rodger. 2010. “Mapping soil surface mineralogy at Tick Hill, North-Western Queensland, Australia, using airborne hyperspectral imagery.” Chap. 18 in *Proximal Soil Sensing*, R.A. Viscarra Rossel, A.B. McBratney, and B. Minasny, Eds. 1: 211-229, Springer Netherlands.

Dawn, S., V. Saxena, and B. Sharma. 2010. “Remote sensing image registration techniques: a survey.” In *Image and Signal Processing. Lecture Notes in Computer Science* 6134: 103-112. Springer Berlin Heidelberg.

Dasgupta, B., and B. N. Chatterji. 1996. “Fourier-Mellin transform based image matching algorithm.” *IETE Journal of Research* 42 (1): 3-9.

Derrode, S., and F. Ghorbel. 2001. “Robust and efficient Fourier–Mellin transform approximations for gray-level image reconstruction and complete invariant description.” *Computer Vision and Image Understanding* 83 (1): 57-78.

Deshmukh, M., and U. Bhosle. 2011. “A survey of image registration.” *International Journal of Image Processing (IJIP)* (5)3: 245-269.

H. Erives, and G. J. Fitzgerald. 2005. “Automated registration of hyperspectral images for precision agriculture.” *Computers and Electronics in Agriculture* 47 (2): 103-119.

H. Erives, and G. J. Fitzgerald. 2006. “Automatic sub-pixel registration for a tunable hyperspectral imaging system.” *In Geoscience and Remote Sensing Symposium, IGARSS 2006, IEEE International Conference on*, 952-955.

Evans, A., and X. Liu. 2006. “A morphological gradient approach to color edge detection.” *IEEE Trans. on Image Processing* 15 (6): 1454-1463.

Fauvel, M., Y. Tarabalka, J. A. Benediktsson, J. Chanussot, and J. C. Tilton.2013. “Advances in spectral–spatial classification of hyperspectral images.” *Proceedings of the IEEE* 101 (3): 652-675.

Gualtieri, J. A., Chettri, S. R., Cromp, R. F., and Johnson, L. F. 1999. “Support vector machine classifiers as applied to AVIRIS data.” *Proc. Eighth JPL Airborne Geoscience Workshop.*

Goshtasby, A. A. 2005. "2-D and 3-D image registration: for medical, remote sensing, and industrial applications." John Wiley and Sons. Hoboken, New Jersey.

Goshtasby, A. A. 2012. "Image registration: Principles, tools and methods." Springer London.

Haboudane, D., J.-R. Miller, E. Pattey, P.J. Zarco-Tejada, and I.B. Strachan. 2004. "Hyperspectral vegetation indices and novel algorithms for predicting green LAI of crop canopies: Modeling and validation in the context of precision agriculture." *Remote Sensing of Environment* 90 (3): 337-352.

Han, Youkyung and Bovolo, Francesca and Bruzzone, Lorenzo. 2015. "An Approach to Fine Coregistration Between Very High Resolution Multispectral Images Based on Registration Noise Distribution." *IEEE Transactions on Geoscience and Remote Sensing* 53 (12): 6650-6662.

Harris, Fredric J. 1978. "On the use of windows for harmonic analysis with the discrete Fourier transform." *Proceedings of the IEEE* 66: 51-83.

Heinrich, M. P., B. W. Papiez, J. A. Schnabel, and H. Handels. 2014. "Multispectral Image Registration Based on Local Canonical Correlation Analysis." In *Medical Image Computing and Computer-Assisted Intervention–MICCAI 2014, Lecture Notes in Computer Science* 8673: 202-209, Springer International Publishing.

Keller, K., A. Averbuch, and M. Israeli. 2005. "Pseudo polar-based estimation of large translations, rotations, and scalings in images." *IEEE Transactions on Image Processing* 14 (1): 12-22.

Ke, Yan, and Rahul Sukthankar. 2004. "PCA-SIFT: A more distinctive representation for local image descriptors." *Computer Vision and Pattern Recognition, 2004. CVPR 2004. Proceedings of the 2004 IEEE Computer Society Conference on.* 2: II-506.

Kern, J. P., M. Pattichis, and S. D. Stearns. 2004. "Registration of image cubes using multivariate mutual information." *In Signals, Systems and Computers, 2004. Conference Record of the Thirty-Seventh Asilomar Conference on, ACSSC* 2: 1645-1649.

Landgrebe, D. 2002. "Hyperspectral image data analysis." *IEEE Signal Processing Magazine* 19 (1): 17-28.

Mahdi, H., and A. Farag. 2002. "Image registration in multispectral data sets. In Image Processing." *Proceedings of the 2002 International Conference on, ICIP 2002*, 2: II-369. IEEE.

Le Moigne, J., N. S. Netanyahu, and R. D. Eastman (Eds.). 2011. "Image registration for remote sensing." Cambridge University Press. Cambridge. UK.

Le Moigne, J., Cole-Rhodes, et al. 2002. "Multiple sensor image registration, image fusion and dimension reduction of earth science imagery." In *Information Fusion, Proceedings of the Fifth International Conference on, ICIF 2002* 2: 999-1006.

Liu, H., B. Guo, and Z. Feng. 2006. "Pseudo-log-polar Fourier transform for image registration." *Signal Processing Letters, IEEE* 13 (1): 17-20.

Lowe, David G. 2004. "Distinctive image features from scale-invariant keypoints." *International journal of computer vision* 60 (2): 91-110.

Pan, W., K. Qin, and Y. Chen. 2009. "An adaptable-multilayer fractional Fourier transform approach for image registration," *Pattern Analysis and Machine Intelligence, IEEE Transactions on* 31 (3): 400-414.

Reddy, B. S., and B. N. Chatterji. 1996. "An FFT-based technique for translation, rotation and scale-invariant image registration." *IEEE Transactions on Image Processing* 5 (8): 1266-1271.

Rey Otero, Ives and Delbracio, Mauricio. 2014. "Anatomy of the SIFT Method." *Image Processing On Line* 4: 370-396.

Rohde, G. K., S. Pajevic, C. Pierpaoli, and P. J. Basser. 2003. "A comprehensive approach for multi-channel image registration." In *Biomedical Image Registration. Lecture Notes in Computer Science* 2717: 214-223. Springer Berlin Heidelberg.

Richards, J. A. 1999. "Remote sensing digital image analysis." Springer. Berlin.

Ruiz-Alzola, J., C. F. Westin, S. K. Warfield, C. Alberola, S. Maier, and R. Kikinis. 2002. "Nonrigid registration of 3D tensor medical data." *Medical image analysis* 6 (2): 143-161.

Stone, H. S., B. Tao, and M. McGuire. 2003. "Analysis of image registration noise due to rotationally dependent aliasing." *Journal of Visual Communication and Image Representation* 14 (2): 114-135.

Vakalopoulou, M., and Karantzalos, K. 2014. "Automatic descriptor-based co-registration of frame hyperspectral data." *Remote Sensing* 6 (4): 3409-3426.

Wang, J., Z. Xu, Z, and J. Zhang. 2013. "Image Registration with Hyperspectral Data Based on Fourier-Mellin Transform." *Geoscience and Remote Sensing Symposium. IGARSS 2006. IEEE International Conference on* 952-955.

Wu, X. X., B. L. Guo, and J. Wang.2009, "Octa-Log-Polar Fourier Transform for Image Registration." *In Information Assurance and Security, IAS'09. Fifth International Conference on* 1: 601-604.

Zhu, Y., Cheng, S., Stanković, V., and Stanković, L. 2013, "Image registration using BP-SIFT." *Journal of Visual Communication and Image Representation* 24 (4): 448-457.

Hyperspectral Remote Sensing Scenes at the University of the Basque Country. [Online]. Available: [`http://www.ehu.eus/ccwintco/index.php?title=Hyperspectral_Remote_Sensing_Scenes`] (2015, June).